Signal-to-noise ratio in correlation plenoptic imaging

Scala, Giovanni, Massaro, Gianlorenzo, D'Angelo, Milena, Garuccio, Augusto, Pascazio, Saverio, et al.

Giovanni Scala, Gianlorenzo Massaro, Milena D'Angelo, Augusto Garuccio, Saverio Pascazio, Francesco V. Pepe, "Signal-to-noise ratio in correlation plenoptic imaging," Proc. SPIE 11347, Quantum Technologies 2020, 1134713 (14 April 2020); doi: 10.1117/12.2555701

SPIE.

Event: SPIE Photonics Europe, 2020, Online Only, France

Signal-to-noise ratio in Correlation Plenoptic Imaging

Giovanni Scala[a,b], Gianlorenzo Massaro[a], Milena D'Angelo[a,b], Augusto Garuccio[a,b], Saverio Pascazio[a,b], and Francesco V. Pepe[a,b]

[a]Dipartimento Interateneo di Fisica, Università degli studi di Bari, I-70126 Bari, Italy
[b]INFN, Sezione di Bari, I-70126 Bari, Italy

ABSTRACT

We review the signal-to-noise properties of two setups for Correlation Plenoptic Imaging (CPI), a novel technique that exploits the correlations of light intensity to perform the typical tasks of plenoptic imaging: refocusing out-of-focus parts of the scene, extending the depth of field, reconstruct 3D objects, As opposed to first-order plenoptic imaging, based on direct intensity measurement, CPI does not entail a loss of spatial resolution. Both setups are based on the properties of chaotic light and employ the concept of ghost imaging in different ways: the first one to image the object, the second one to image the focusing element. We show that the SNR can be easier to control in the second CPI scheme, in which the object is focused by a lens.

Keywords: 3D imaging, correlations of light, correlation imaging, quantum imaging, plenoptic imaging

1. INTRODUCTION

The recently established technique of Plenoptic Imaging (PI) is based on the idea of recording at the same time the spatial distribution and propagation direction of light.[1] Although the first feasible proposal to apply plenoptic imaging to digital cameras dates back to the mid-2000s,[2] the seminal intuition can be attributed to Lippmann[3] one century earlier. PI is currently employed in a broad range of applications, that include stereoscopy,[1,4,5] microscopy,[6–9] particle image velocimetry,[10] particle tracking and sizing,[11] and wavefront sensing.[12–14] Since plenoptic devices are able to simultaneously acquire 2D images from multiple perspectives, they are considered among the fastest and most promising methods for 3D imaging,[15] as shown by the very recent use in imaging of animal neuronal activity,[9] surgical robotics,[16] endoscopy[17] and blood-flow visualization.[18] While currently available plenoptic imaging devices, based on first-order intensity measurement on a single detector,[2,19,20] entail an unavoidable loss of spatial resolution, this problem was overcome in Correlation Plenoptic Imaging (CPI) by exploiting intensity correlations of either chaotic light[21–24] or entangled photon pairs.[25] The key idea of CPI, inspired by ghost imaging with chaotic and entangled light,[26–33] is to encode information of the scene and the direction of light in two separate sensors: the desired information emerges by evaluating intensity correlations, and the image resolution can still reach the diffraction limit. CPI is a promising case of a technology developed in the field of quantum imaging, that enables to go beyond the capabilities of standard imaging and interferometry devices.[?,26,34–41]

Though the tradeoff between spatial and directional resolution can be overcome by using CPI instead of traditional plenoptic imaging, the former has the disadvantage of requiring the reconstruction of the source statistics, thus losing the single-shot advantage of standard plenoptic imaging. The signal-to-noise ratio (SNR) improves with the number of frames; however, to aim at performing real-time imaging, the number of acquired frames should be as small as possible. The choice of the optimal frame number is particularly delicate in the case of ghost images with chaotic light, characterized by a well-known tradeoff between resolution and SNR.[42–45] Ways to mitigate such tradeoff involve image analysis techniques[46,47] and alternative measurement schemes.[48] In this paper, we review the SNR properties of two different CPI schemes based on the properties of chaotic light and designed according to complementary concepts (see Fig. 1):[49] the first one (SETUP1) exploits ghost imaging to obtain the image of the object, and standard imaging to get directional information, while in the second one (SETUP2) the object is imaged by a lens, and ghost imaging is used to obtain directional information.

Send correspondence to M. D'Angelo. E-mail: milena.dangelo@uniba.it

Quantum Technologies 2020, edited by Eleni Diamanti, Sara Ducci, Nicolas Treps, Shannon Whitlock,
Proc. of SPIE Vol. 11347, 1134713 · © 2020 SPIE · CCC code: 0277-786X/20/$21 · doi: 10.1117/12.2555701

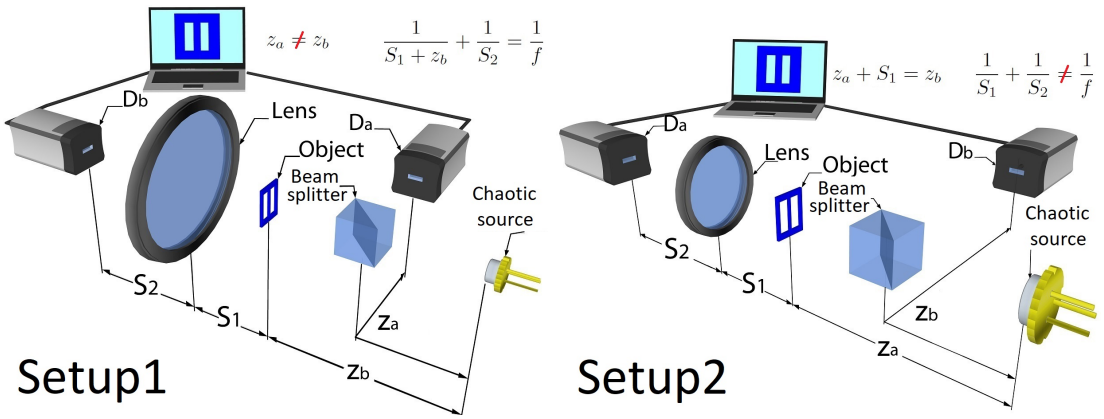

Figure 1. Schematic representation of two setups that enable to perform plenoptic imaging by measuring the correlation of intensity fluctuations between points on two spatially resolving detectors D_a and D_b. Both setups are illuminated by chaotic light, that is split in two paths by a beam splitter, and feature a transmissive object and a lens of focal length f. In SETUP1 (upper panel), the chaotic source is focused by the lens on detector D_b, while the "ghost" image of the object emerges in correspondence of D_a from the average correlation $\Gamma(\boldsymbol{\rho}_a,\boldsymbol{\rho}_b)=\langle\Delta i(\boldsymbol{\rho}_a)\Delta i(\boldsymbol{\rho}_b)\rangle$. SETUP2 (lower panel) is based on a different working principle: the image of the object is formed by the lens on D_a, while the ghost image of the lens is retrieved in correspondence of D_b by computing correlations between D_a and D_b. In both cases, encoding these two images in the correlation function of Eq. (1) provides information on the direction of light in the setup, giving the possibility to recover the image of the object even if the focusing conditions (namely, $z_b=z_a$ for SETUP1, and $1/S_1+1/S_2=1/f$ for SETUP2) are not satisfied.

2. CORRELATION PLENOPTIC IMAGING SCHEMES

We will consider the two setups (SETUP1 and SETUP2) represented in Fig. 1, both capable of performing, CPI.[21,23,24] The two schemes are different in the way ghost imaging is employed to obtain an image of either the object plane (SETUP1) or the focusing element (SETUP2). The common feature of the two setups is the fact that light emitted by a chaotic source is split in two paths a and b by a beam splitter (BS), and is recorded at the end of each path by the high-resolution detectors D_a and D_b. An object is always placed in one of the two paths. More specifically, intensity patterns $I_A(\boldsymbol{\rho}_a)$ and $I_B(\boldsymbol{\rho}_b)$, with $\boldsymbol{\rho}_{a,b}$ the coordinate on each detector plane, are recorded in time to reconstruct the correlation function

$$\Gamma(\boldsymbol{\rho}_a,\boldsymbol{\rho}_b)=\langle\Delta I_A(\boldsymbol{\rho}_a)\Delta I_B(\boldsymbol{\rho}_b)\rangle, \tag{1}$$

with $\Delta I_{A,B}(\boldsymbol{\rho}_{a,b})=I_{A,B}(\boldsymbol{\rho}_{a,b})-\langle I_{A,B}(\boldsymbol{\rho}_{a,b})\rangle$. The expectation value in (1) must be evaluated over the source statistics, but it can be approximated by the time average of the product of the intensity fluctuations, provided the source is stationary and ergodic.[50] In the discussed setups, the images of the object plane and of the focusing element aperture will be simultaneously encoded in $\Gamma_{AB}(\boldsymbol{\rho}_a,\boldsymbol{\rho}_b)$.

In SETUP1, an image of the object can be obtained only by measuring intensity correlations between D_a and D_b. Along path a (the reflected path in figure), light directly impinges on detector D_a, placed at an optical distance z_a from the source. In path b (the transmitted path in figure), a transmissive object lies at a distance z_b from the source. A thin lens of focal length f is placed between the object and the detector D_b, at a distance S_1 from the former and S_2 from the latter. Such distances are chosen in order to focus the source on D_b with magnification $M=S_2/(S_1+z_b)$, hence, they satisfy the thin-lens equation $1/S_2+1/(S_1+z_b)=1/f$. In the case $z_b=z_a$, measurement of the correlation function $\Gamma(\boldsymbol{\rho}_a,\boldsymbol{\rho}_b)$ and direct integration over $\boldsymbol{\rho}_b$ provides the *focused* ghost image of the object.[29]

In SETUP2, the image of the lens is recovered from intensity correlations between D_a and D_b. Along path b (the reflected path in figure), light directly impinges on the detector D_b, placed at an optical distance z_b from the source. In path a (the transmitted path in figure), the transmissive object is placed at a distance z_a from the source. The thin lens of focal length f lies between the object and the detector D_a, at a distance S_1 from the former and S_2 from the latter. In this case, the setup is designed to obtain a focused ghost image of the

lens on the detector D_b: therefore, distances are fixed in order to satisfy $z_b = z_a + S_1$. The object-to-lens and lens-to-D_a distances are arbitrary. However, it is intuitive that, if $S_2 = S_2^f$, such that $1/S_1 + 1/S_2^f = 1/f$, the image of the object will be sharply focused on D_a.

The refocusing capability of both setups is determined by the fact that the correlation function (1) encodes multiple coherent images of the object, one for each point $\boldsymbol{\rho}_b$ on D_b. The images corresponding to different pixels on D_b are generally displaced with respect to each other, unless a focusing condition is satisfied. In the focused case, integration over detector D_b yields an incoherent image. In the out-of-focus cases, the collected coherent images need to be realigned *before* integrating over D_b, following

$$\Sigma_{\mathrm{ref}}(\boldsymbol{\rho}_a) = \langle \mathcal{S}_{(\alpha,\beta)}(\boldsymbol{\rho}_a) \rangle, \tag{2}$$

with

$$\mathcal{S}_{(\alpha,\beta)}(\boldsymbol{\rho}_a) = \int \mathrm{d}^2\boldsymbol{\rho}_b \Delta I_A(\alpha\boldsymbol{\rho}_a + \beta\boldsymbol{\rho}_b)\Delta I_B(\boldsymbol{\rho}_b). \tag{3}$$

The parameters (α, β), that approach $(1, 0)$ at focus, are properly chosen to realign the coherent images depending on the setup, and read

$$(\alpha,\beta) = \begin{cases} \left(\dfrac{z_a}{z_b}, -\dfrac{1}{M}\left(1 - \dfrac{z_a}{z_b}\right)\right) & \text{for SETUP1,} \\ \left(\dfrac{S_2}{S_2^f}, 1 - \dfrac{S_2}{S_2^f}\right) & \text{for SETUP2.} \end{cases} \tag{4}$$

It is evident that, when the focusing conditions are fulfilled, there is no need to shift and rescale the first argument of Γ, and the high resolution of detector D_b plays no role. In all other cases, the spatial resolution of D_b is essential to reconstruct the image of an out-of-focus object, which, by direct integration over D_b, would appear blurred and degraded.

3. FLUCTUATIONS AND SNR

The objective of this paper is to estimate the signal-to-noise ratio characterizing the refocused images retrieved in SETUP1 and SETUP2. To this end, we shall analyze the fluctuations of the refocused observable $\mathcal{S}_{(\alpha,\beta)}(\boldsymbol{\rho}_a)$, defined in Eq. (3), around its average $\Sigma_{\mathrm{ref}}(\boldsymbol{\rho}_a)$, namely

$$\mathcal{F}(\boldsymbol{\rho}_a) = \langle \mathcal{S}_{(\alpha,\beta)}(\boldsymbol{\rho}_a)^2 \rangle - \langle \mathcal{S}_{(\alpha,\beta)}(\boldsymbol{\rho}_a) \rangle^2 = \int \mathrm{d}^2\boldsymbol{\rho}_{b1}\mathrm{d}^2\boldsymbol{\rho}_{b2}\Phi(\boldsymbol{\rho}_a, \boldsymbol{\rho}_{b1}, \boldsymbol{\rho}_{b2}), \tag{5}$$

with Φ determined by the local fluctuations of the intensity correlations [see Eq. (3)]. Let us assume that N_f frames are collected in time to evaluate the expectation value (2). Supposing their statistical independence, the root-mean-square error affecting the evaluation of $\Sigma_{\mathrm{ref}}(\boldsymbol{\rho}_a)$ can be estimated by $\sqrt{\mathcal{F}(\boldsymbol{\rho}_a)/N_f}$. We therefore define the quantity

$$R(\boldsymbol{\rho}_a) = \sqrt{N_f}\frac{\Sigma_{\mathrm{ref}}(\boldsymbol{\rho}_a)}{\sqrt{\mathcal{F}(\boldsymbol{\rho}_a)}}. \tag{6}$$

as the signal-to-noise ratio.

A scalar model of the electromagnetic field, in which the effects of polarization are neglected, will be adopted, and we will assume that the radiation emission by the source is an approximately Gaussian random process, stationary and ergodic. In particular, in the approximation of small transverse coherence length σ_g, the field $V_S(\boldsymbol{\rho}_s)$ at a point $\boldsymbol{\rho}_s$ on the source will be characterized by the equal-time correlator[50]

$$W_S(\boldsymbol{\rho}_s, \boldsymbol{\rho}_s') = \langle V_S(\boldsymbol{\rho}_s) V_S^*(\boldsymbol{\rho}_s') \rangle = 2\pi\sigma_g^2 I_s \mathrm{e}^{-\frac{\rho_s^2}{2\sigma_i^2}} \delta^{(2)}(\boldsymbol{\rho}), \tag{7}$$

with I_s the peak intensity and σ_i the width of the intensity profile. The computation of both the signal (2) and the fluctuations around its mean value requires higher-order field correlators, for which we assume a Gaussian behavior, namely[51]

$$\langle \prod_{j=1}^{n} V_S(\boldsymbol{\rho}_j) V_S^*(\boldsymbol{\rho}'_j) \rangle = \sum_{\mathrm{P}} \prod_{j=1}^{n} \langle V_S(\boldsymbol{\rho}_j) V_S^*(\mathrm{P}\boldsymbol{\rho}'_j) \rangle, \tag{8}$$

with P a permutation of the primed indexes, for the correlators that involve an equal number of V's and V^*'s. All other expectation values, including $\langle V \rangle$ and $\langle V^* \rangle$, are vanishing. Propagation from the source to the detectors along the two paths a and b is instead deterministic. In free space, the field evaluated on a plane at a generic longitudinal position z, assumed to be monochromatic with frequency ω and wavenumber $k = \omega/c$, is related to the field at $z_0 < z$ by the paraxial transfer function:[52]

$$V(\boldsymbol{\rho}; z) = \frac{-\mathrm{i}k}{2\pi(z - z_0)} \int \mathrm{d}^2\boldsymbol{\rho}' V(\boldsymbol{\rho}'; z_0) \mathrm{e}^{\mathrm{i}k\left[\frac{(\boldsymbol{\rho}-\boldsymbol{\rho}')^2}{2(z-z_0)} + (z - z_0)\right]}. \tag{9}$$

The correlators between fields $V_A(\boldsymbol{\rho}_a)$ and $V_B(\boldsymbol{\rho}_b)$ inherit the factorization property (8) from fields on the source. In particular, the correlation of intensity fluctuations between the two detectors, defined in Eq. (1), reads

$$\Gamma(\boldsymbol{\rho}_a, \boldsymbol{\rho}_b) = \left| \langle V_A(\boldsymbol{\rho}_a) V_B^*(\boldsymbol{\rho}_b) \rangle \right|^2. \tag{10}$$

In both setups, $\mathcal{F}(\boldsymbol{\rho}_a)$ is determined with good approximation by the contribution that features only the self-correlations:

$$\mathcal{F}_0(\boldsymbol{\rho}_a) = \int \mathrm{d}^2\boldsymbol{\rho}_{b1} \mathrm{d}^2\boldsymbol{\rho}_{b2} \left| \langle V_A(\alpha\boldsymbol{\rho}_a + \beta\boldsymbol{\rho}_{b1}) V_A^*(\alpha\boldsymbol{\rho}_a + \beta\boldsymbol{\rho}_{b2}) \rangle \right|^2 \left| \langle V_B(\boldsymbol{\rho}_{b1}) V_B^*(\boldsymbol{\rho}_{b2}) \rangle \right|^2. \tag{11}$$

Other contributions are typically suppressed as

$$\frac{|\mathcal{F} - \mathcal{F}_0|}{\mathcal{F}_0} \sim \frac{1}{\mathcal{N}_b}, \tag{12}$$

with $\mathcal{N}_b$ the number of transverse modes that propagate towards the detector D_b. Therefore, in the following, we shall approximate $\mathcal{F} \simeq \mathcal{F}_0$ when computing the SNR.

In SETUP1 (Fig. 1, upper panel), calling $A(\boldsymbol{\rho})$ the aperture function of the object, and neglecting the finite pupil size of the lens, the combination of free propagation (9), transmission through object and lens,[52] and assumptions on source statistics (7)-(8),

$$\Gamma(\boldsymbol{\rho}_a, \boldsymbol{\rho}_b) = K_{AB} \frac{\sigma_i^4}{1 + k^2\sigma_i^4 \left(\frac{1}{z_a} - \frac{1}{z_b}\right)^2} \left| \int \mathrm{d}^2\boldsymbol{\rho}_o A(\boldsymbol{\rho}_o) \mathrm{e}^{-\gamma_a\left(\frac{\boldsymbol{\rho}_a}{\alpha} - \boldsymbol{\rho}_o\right)^2 - \mathrm{i}\gamma_b \boldsymbol{\rho}_b \cdot \boldsymbol{\rho}_o} \right|^2, \tag{13}$$

where K_{AB} is an irrelevant constant, $\alpha = z_a/z_b$ as in (4), and

$$\gamma_a = \frac{k^2\sigma_i^2}{2z_b^2} \left[1 + \mathrm{i}k\sigma_i^2 \left(\frac{1}{z_a} - \frac{1}{z_b}\right)\right]^{-1}, \quad \gamma_b = \frac{k}{M z_b}, \tag{14}$$

The result (13) shows that, by varying $\boldsymbol{\rho}_b$, a collection of coherent images of the object is obtained on D_a.

Combining Eq. (13) with the definitions (2)–(4), we determine the refocused image

$$\Sigma_{\mathrm{ref}}(\boldsymbol{\rho}_a) = \frac{\pi z_b^2 \sigma_i^2}{\delta^2 k^2} K_{AB}^{(2)} \int \mathrm{d}^2\boldsymbol{\rho}_1 \int \mathrm{d}^2\boldsymbol{\rho}_2 A^*(\boldsymbol{\rho}_a - \boldsymbol{\rho}_1) A(\boldsymbol{\rho}_a - \boldsymbol{\rho}_2) \mathrm{e}^{\mathrm{i}\frac{\gamma_b(\boldsymbol{\rho}_1^2 - \boldsymbol{\rho}_2^2)}{2\delta} - \left(\frac{\gamma_r}{2} + \frac{(\gamma_b - 2\delta\gamma_i)^2}{8\delta^2\gamma_r}\right)(\boldsymbol{\rho}_1 - \boldsymbol{\rho}_2)^2}, \tag{15}$$

with $\delta = (1 - z_b/z_a)/M$. This quantity is regular in the focused limit $\delta \to 0$, where

$$\Sigma_{\mathrm{ref}}(\boldsymbol{\rho}_a)\big|_{z_b = z_a} = \int \mathrm{d}^2\boldsymbol{\rho}_b \Gamma(\boldsymbol{\rho}_a, \boldsymbol{\rho}_b) \sim \int \mathrm{d}^2\boldsymbol{\rho}_o |A(\boldsymbol{\rho}_o)|^2 \exp\left(-\frac{(\boldsymbol{\rho}_a - \boldsymbol{\rho}_o)^2}{\sigma_A^2}\right), \tag{16}$$

which is exactly the unit-magnification incoherent image obtained in the case of lensless ghost imaging,[29,44] whose point-spread function is determined by the squared Fourier transform of the source intensity profile.

Defining

$$\sigma_A = \frac{z_a}{k\sigma_i}, \quad \sigma_B = \frac{z_b}{k\sigma_i} \tag{17}$$

as the transverse coherence lengths on the planes at a distance z_a and z_b, respectively, from the source, the dominant contribution to the variance of the correlation of the intensity fluctuations, defined in Eq. (11), reads

$$\mathcal{F}_0(\boldsymbol{\rho}_a) = 4\pi^3 \left(K_{AB}^{(1)} \frac{\sigma_A \sigma_i^4}{\gamma_b \beta} \right)^2 \int \Big(\prod_{j=1}^{3} \mathrm{d}^2\boldsymbol{\rho}_j \Big) A(\boldsymbol{\rho}_1) A^*(\boldsymbol{\rho}_2) A(\boldsymbol{\rho}_3) A^*(\boldsymbol{\rho}_1 + \boldsymbol{\rho}_3 - \boldsymbol{\rho}_2) \mathrm{e}^{-\frac{(\boldsymbol{\rho}_2 - \boldsymbol{\rho}_3)^2}{\sigma_B^2} - \frac{(\boldsymbol{\rho}_1 - \boldsymbol{\rho}_2)^2}{4\sigma_i^2 (1 - z_b/z_a)^2}}, \tag{18}$$

The most interesting feature of such quantity is its independence on the coordinate $\boldsymbol{\rho}_a$ on D_a. Therefore, not only the signal $\Sigma_{\mathrm{ref}}(\boldsymbol{\rho}_a)$ is noisy, but it is also superposed to a background noise of the same intensity as local noise. Such constant background noise stems from the fact that the intensity profile of light impinging on D_a is, in the case of SETUP1, completely unrelated to the spatial profile of the signal $\Sigma_{\mathrm{ref}}(\boldsymbol{\rho}_a)$.

Let us evaluate and discuss some limiting cases, adopting the geometrical-optics approximation to simplify the integrals. In the focused case, in which $z_a = z_b$ and $\sigma_A = \sigma_B$ the value of the SNR reduces to

$$R(\boldsymbol{\rho}_a)|_{z_b = z_a} \simeq \sqrt{N_f \frac{\pi \sigma_B^2}{\int \mathrm{d}^2\boldsymbol{\rho} |A(\boldsymbol{\rho})|^4}} |A(\boldsymbol{\rho}_a)|^2. \tag{19}$$

The above expression highlights the dependence of the SNR on the ratio between the coherence area of light on the object and the effective area of the object itself, coinciding with the actual area in the case of binary transmission functions. Since the same coherence area determines the resolution through (16), this result entails the well-known tradeoff between resolution and SNR typical of ghost imaging.[42–45] In the far out-of-focus regime, when $\sigma_i |1 - z_b/z_a|$ is larger than the size of the object, the signal-to-noise ratio yields

$$R(\boldsymbol{\rho}_a) \simeq \sqrt{N_f} \lambda z_b \left| 1 - \frac{z_b}{z_a} \right| \frac{|A(\boldsymbol{\rho}_a)|^2}{\int \mathrm{d}^2\boldsymbol{\rho} |A(\boldsymbol{\rho})|^2}, \tag{20}$$

with $\lambda = 2\pi/k$ the light wavelength. This expression shows a less trivial dependence on the longitudinal position z_b of the refocused plane, but can still be interpreted in terms of the resolution-SNR tradeoff. Actually, as discussed in,[21,24] a good estimate of the resolution of the refocused image is given by $\Delta x = (\lambda z_b/a)|1 - z_b/z_a|$, where a is the typical linear size of the smallest transmissive parts of the object. Notice, however, that the inverse dependence on the effective area of the object has changed with respect to the focused case (19). As a rule of thumb, we can estimate the SNR of refocused images as

$$\frac{R^{(g)}(\boldsymbol{\rho}_a)}{\sqrt{N_f}} \sim \sqrt{\frac{a^2}{A_{\mathrm{obj}}}} \sqrt{\frac{(\Delta x)^2}{A_{\mathrm{obj}}}} |A(\boldsymbol{\rho}_a)|^2, \tag{21}$$

a result that depends on the product of the ratios (resolution cell)/(total area) and (smallest detail area)/(total area).

In SETUP2, we consider a finite-size pupil $P(\boldsymbol{\rho})$ of the lens, that determines the spatial resolution, and assume that the finite size of the source does not affect in a relevant way the correlation measurement of the intensity fluctuations. In this way, the correlation of intensity fluctuations reads

$$\Gamma(\boldsymbol{\rho}_a, \boldsymbol{\rho}_b) = \left(\frac{z_a(z_a + S_1)}{k S_1} \right)^2 K_{AB}^{(2)} \left| \int \mathrm{d}^2\boldsymbol{\rho}_o A(\boldsymbol{\rho}_o) \tilde{P}_\beta \Big(\frac{\boldsymbol{\rho}_o}{S_1} + \frac{\boldsymbol{\rho}_a}{S_2} \Big) \mathrm{e}^{\frac{\mathrm{i}k}{S_1} \boldsymbol{\rho}_o \cdot \boldsymbol{\rho}_b} \right|^2, \tag{22}$$

where

$$\tilde{P}_\beta(\boldsymbol{q}) = \int \mathrm{d}^2\boldsymbol{\rho}_\ell P(\boldsymbol{\rho}_\ell) \exp\left(\frac{\mathrm{i}k\beta}{2S_2} \boldsymbol{\rho}_\ell^2 - \mathrm{i}k\boldsymbol{q} \cdot \boldsymbol{\rho}_\ell \right) \tag{23}$$

coincides with the Fourier transform of the pupil function in the focused case, obtained when $S_2 = S_2^f = (1/f - 1/S_1)^{-1}$ and $\beta = 0$, and $K_{AB}^{(2)}$ is an irrelevant constant. The refocused image, defined by (α, β) in the second line of Eq. (4), reads

$$\Sigma_{\mathrm{ref}}(\boldsymbol{\rho}_a) = \left(\frac{2\pi z_a(z_a+S_1)}{k^2}\right)^2 K_{AB} \int \mathrm{d}^2\boldsymbol{\rho}_1 \mathrm{d}^2\boldsymbol{\rho}_2 \mathrm{d}^2\boldsymbol{\rho}_o P^*(\boldsymbol{\rho}_1) P(\boldsymbol{\rho}_2) A^*(\boldsymbol{\rho}_o) A\Big(\boldsymbol{\rho}_o + \frac{\beta S_1}{S_2}(\boldsymbol{\rho}_2 - \boldsymbol{\rho}_1)\Big) \times \mathrm{e}^{-\frac{\mathrm{i}k\beta}{2S_2}(\boldsymbol{\rho}_2-\boldsymbol{\rho}_1)^2 + \mathrm{i}k\left(\frac{\boldsymbol{\rho}_b}{S_2^f} + \frac{\boldsymbol{\rho}_o}{S_1}\right)\cdot(\boldsymbol{\rho}_2-\boldsymbol{\rho}_1)}. \quad (24)$$

In the focused case $\beta = 0$, the above expression becomes proportional to the first-order incoherent image of the object transmission function, with absolute magnification $\mu = S_2^f/S_1$. Also in this case, the dominant contribution to the variance of $\mathcal{S}_{(\alpha,\beta)}$ can be evaluated by considering the autocorrelations. However, the computation of (11) must take into account the finite size of the detector D_b, since, integrating without bounds on $\boldsymbol{\rho}_b$ would yield a divergent result. Since the role of D_b is to detect the ghost image of the lens, which is characterized by unit magnification, the optimal size of this detector is given by the size of the lens. Following these considerations and assuming the limit of large source width σ_i, one obtains

$$\mathcal{F}_0(\boldsymbol{\rho}_a) = 4\pi^3\sigma_i^2 \left(K_{AB}^{(2)} \frac{z_a^2(z_a+S_1)}{k^3}\right)^2 \int_{\mathrm{D}_b} \mathrm{d}^2\boldsymbol{\rho}_b \left(\int \mathrm{d}^2\boldsymbol{\rho}_o |A(\boldsymbol{\rho}_o)|^2 \left|\tilde{P}_\beta\Big(\frac{\boldsymbol{\rho}_o}{S_1} + \frac{\alpha\boldsymbol{\rho}_a + \beta\boldsymbol{\rho}_b}{S_2}\Big)\right|^2\right)^2. \quad (25)$$

In the focused case, the integral in (25) is trivially proportional to the squared intensity, which is $\boldsymbol{\rho}_a$-dependent, as opposed to the case of SETUP1. In the general case, the analytic evaluation of (25) can become impossible when considering the actual detector area as the integration domain. However, the computation could be performed by regularizing the integral with a Gaussian envelope function $\exp(-\pi\boldsymbol{\rho}_b^2/A_{\mathrm{D}_b})$, where A_{D_b} is the area of detector D_b (or, better, the area of the part of the detector that accommodates the image of the lens). The spatial behavior of the variance $\mathcal{F}_0$ is now much less trivial than the constant behavior found in SETUP1. Actually, in the focused limit $S_2 \to S_2^f$, the integrand of (25), coinciding with the squared and shifted incoherent image of the object, becomes independent of $\boldsymbol{\rho}_b$. Therefore, at least in the focused case, *noise is proportional to the signal*. Such feature is due to the fact that, as opposed to the case of ghost imaging, the field transmitted by the object is focused on the spatial detector D_a. In the opposite limit of large defocusing, instead, the spatial dependence of $\mathcal{F}_0$ becomes gradually irrelevant, implying that the measurement of $\Sigma_{\mathrm{ref}}(\boldsymbol{\rho}_a)$ becomes characterized by a uniform background noise.

The geometrical-optics approximation provides, in the focused case, the estimate

$$R(\boldsymbol{\rho}_a)|_{S_2=S_2^f} \simeq 2\sigma_B \sqrt{N_f \frac{\pi}{A_{\mathrm{D}_b}}}, \quad (26)$$

which is $\boldsymbol{\rho}_a$-independent, since noise is proportional to the signal. The constant SNR in (26) is essentially the square root of the ratio of the coherence area $\sim \sigma_B^2$ on D_b and the area A_{D_b} of the same detector, which can also be interpreted as (coherence area on the lens)/(area of the lens), in perfect analogy with Eq. (19), after replacing the object with the lens. The SNR thus coincides with the one expected for the ghost image of the lens. However, it does not depend on the magnitude of the signal. In the out-of-focus case, a background noise emerges, and the SNR becomes similar in form to (20), reading

$$R(\boldsymbol{\rho}_a) \simeq 2\sigma_B \sqrt{N_f \frac{\pi}{A_{\mathrm{D}_b}}} \left(\frac{1 - S_2/S_2^f}{S_2/S_1}\right)^2 \frac{\int \mathrm{d}^2\boldsymbol{\rho} |P(\boldsymbol{\rho})|^2}{\int \mathrm{d}^2\boldsymbol{\rho} |A(\boldsymbol{\rho})|^2} |P(0)|^2 \left|A\left(-\frac{\boldsymbol{\rho}_a}{\mu}\right)\right|^2. \quad (27)$$

The signal-to-noise ratio increases quadratically with defocusing, providing a generally more favorable picture compared to SETUP1. A good rule to estimate the order of magnitude of the refocused image SNR is therefore represented by

$$\frac{R(\boldsymbol{\rho}_a)}{\sqrt{N_f}} \sim \Big(\frac{S_2/S_1}{1 - S_2/S_2^f}\Big)^2 \sqrt{\frac{\sigma_B^2}{A_{\mathrm{lens}}} \frac{A_{\mathrm{lens}}}{A_{\mathrm{obj}}}} \left|A\left(-\frac{\boldsymbol{\rho}_a}{\mu}\right)\right|^2, \quad (28)$$

where we have assumed that the area of the detector is matched to the area of the lens.

Considering the discussed results for SETUP1 and SETUP2, the latter are generally more advantageous than for the former. In the focused case, SETUP2 is characterized by a suppression of background noise, which is a typical feature affecting the ghost image obtained in SETUP1. Moreover, noise in SETUP1 increases with improving spatial resolution on the object, thus entailing a trade-off between resolution and SNR trade-off. In the out-of-focus case, background noise is present in both configurations. However, in SETUP1 it depends on small quantities, namely the ratios $(\Delta x)^2/A_{\rm obj}$ between the area of an effective resolution cell and the total area of the object, and $a^2/A_{\rm obj}$, where the numerator is the area corresponding to the size a of the finest details of the object. In SETUP2, instead, we find that the SNR depends also on the ratio $A_{\rm lens}/A_{\rm obj}$, that is not necessarily small. Therefore, we expect that a smaller number of frames is needed to achieve the same resolution in SETUP2 compared to SETUP1.

4. CONCLUSIONS

For the considered CPI schemes, we have reviewed results that provide rules to determine the scaling of the SNR with the number of frames, and consequently to adjust the number of frames needed for an imaging process that is at the same time fast and accurate. The optimization of the acquisition time is of capital importance in view of all those cases in which the retrieval of correlations, necessary to perform CPI, is particularly difficult. In our future research, we plan to extend our analysis to the case in which CPI is performed with entangled photons[25] and to setups adapted to microscopy.

ACKNOWLEDGMENTS

This work was supported by Istituto Nazionale di Fisica Nucleare (INFN) projects "PICS" and "QUANTUM", and by PON ARS 01_00141 "CLOSE – Close to Earth" of Ministero dell'Istruzione, dell'Università e della ricerca (MIUR).

REFERENCES

[1] Adelson, E. H. and Wang, J. Y., "Single lens stereo with a plenoptic camera," *IEEE Trans. Pattern Anal. Mach. Intell.* **14**, 99 (1992).

[2] Ng, R., Levoy, M., Brédif, M., Duval, G., Horowitz, M., and Hanrahan, P., "Light field photography with a hand-held plenoptic camera," *Stanford University Computer Science Tech Report CSTR 2005-02* .

[3] Lippmann, G., "épreuves réversibles donnant la sensation du relief," *J. Phys. Theor. Appl.* **7**, 821 (1908).

[4] Muenzel, S. and Fleischer, J. W., "Enhancing layered 3d displays with a lens," *Appl. Opt.* **52**, D97 (2013).

[5] Levoy, M. and Hanrahan, P., "Light field rendering," in [*Proceedings of the 23rd Annual Conference on Computer Graphics and Interactive Technique*], 31–42 (1996).

[6] Levoy, M., Ng, R., Adams, A., Footer, M., and Horowitz, M., "Light field microscopy," *ACM Trans. Graph.* **25**, 924 (2006).

[7] Broxton, M., Grosenick, L., Yang, S., Cohen, N., Andalman, A., Deisseroth, K., and Levoy, M., "Wave optics theory and 3-d deconvolution for the light field microscope," *Opt. Express* **21**, 25418 (2013).

[8] Glastre, W., Hugon, O., Jacquin, O., de Chatellus, H. G., and Laco, E., "Demonstration of a plenoptic microscope based on laser optical feedback imaging," *Opt. Express* **21**, 7294 (2013).

[9] Prevedel, R., Yoon, Y.-G., Hoffmann, M., Pak, N., Wetzstein, G., Kato, S., Schrödel, T., Raskar, R., Zimmer, M., Boyden, E. S., and Vaziri, A., "Simultaneous whole-animal 3d imaging of neuronal activity using light-field microscopy," *Nat. Methods* **11**, 727 (2014).

[10] Fahringer, T. W., Lynch, K. P., and Thurow, B. S., "Volumetric particle image velocimetry with a single plenoptic camera," *Meas. Sci. Technol.* **26**, 115201 (2015).

[11] Hall, E. M., Thurow, B. S., and Guildenbecher, D. R., "Comparison of three-dimensional particle tracking and sizing using plenoptic imaging and digital in-line holography," *Appl. Opt.* **55**, 6410 (2016).

[12] Lv, Y., Wang, R., Ma, H., Zhang, X., Ning, Y., and Xu, X., "Su-g-iep4-09: Method of human eye aberration measurement using plenoptic camera over large field of view," *Med. Phys.* **43**, 3679 (2016).

[13] Wu, C., Ko, J., and Davis, C. C., "Using a plenoptic sensor to reconstruct vortex phase structures," *Opt. Lett.* **41**, 3169 (2016).
[14] Wu, C., Ko, J., and Davis, C. C., "Imaging through strong turbulence with a light field approach," *Opt. Express* **24**, 11975 (2016).
[15] Xiao, X., Javidi, B., Martinez-Corral, M., and Stern, A., "Advances in three-dimensional integral imaging: sensing, display, and application," *Appl. Opt.* **52**, 546 (2013).
[16] Shademan, A., Decker, R. S., Opfermann, J., Leonard, S., Kim, P. C., and Krieger, A., "Plenoptic cameras in surgical robotics: Calibration, registration, and evaluation," in [*Proceedings of the 2016 IEEE International Conference on Robotics and Automation (ICRA)*], 708–714 (2016).
[17] Le, H. N., Decker, R., Opferman, J., Kim, P., Krieger, A., and Kang, J. U., "3-d endoscopic imaging using plenoptic camera," in [*CLEO: Applications and Technology*], AW4O.2 (2016).
[18] Carlsohn, M. F., Kemmling, A., Petersen, A., and Wietzke, L., "3d real-time visualization of blood flow in cerebral aneurysms by light field particle image velocimetry," *Proc. SPIE* **9897**, 989703 (2016).
[19] Georgiev, T. G. and Lumsdaine, A., "Focused plenoptic camera and rendering," *J. Electron. Imaging* **19**, 021106 (2010).
[20] Georgiev, T. and Lumsdaine, A., "The multifocus plenoptic camera," *Proc. SPIE* **8299**, 829908 (2012).
[21] D'Angelo, M., Pepe, F. V., Garuccio, A., and Scarcelli, G., "Correlation plenoptic imaging," *Phys. Rev. Lett.* **116**, 223602 (2016).
[22] Pepe, F. V., Scarcelli, G., Garuccio, A., and D'Angelo, M., "Plenoptic imaging with second-order correlations of light," *Quantum Meas. Quantum Metrol.* **3**, 20 (2016).
[23] Pepe, F. V., Vaccarelli, O., Garuccio, A., Scarcelli, G., and D'Angelo, M., "Exploring plenoptic properties of correlation imaging with chaotic light," *J. Opt.* **19**, 114001 (2017).
[24] Pepe, F. V., Lena, F. D., Mazzilli, A., Edrei, E., Garuccio, A., Scarcelli, G., and D'Angelo, M., "Diffraction-limited plenoptic imaging with correlated light," *Phys. Rev. Lett.* **119**, 243602 (2017).
[25] Pepe, F. V., Lena, F. D., Garuccio, A., Scarcelli, G., and D'Angelo, M., "Correlation plenoptic imaging with entangled photons," *Technologies–Open Access Multidisciplinary Engineering Journal* **4**, 17 (2016).
[26] Pittman, T. B., Shih, Y. H., Strekalov, D. V., and Sergienko, A. V., "Optical imaging by means of two-photon quantum entanglement," *Phys. Rev. A* **52**, R3429 (1995).
[27] Gatti, A., Brambilla, E., Bache, M., and Lugiato, L. A., "Ghost imaging with thermal light: comparing entanglement and classical correlation," *Phys. Rev. Lett.* **93**, 093602 (2004).
[28] Valencia, A., Scarcelli, G., D'Angelo, M., and Shih, Y., "Two-photon imaging with thermal light," *Phys. Rev. Lett.* **94**, 063601 (2005).
[29] Scarcelli, G., Berardi, V., and Shih, Y., "Can two-photon correlation of chaotic light be considered as correlation of intensity fluctuations?," *Phys. Rev. Lett.* **96**, 063602 (2006).
[30] Bennink, R. S., Bentley, S. J., Boyd, R. W., and Howell, J. C., "Quantum and classical coincidence imaging," *Phys. Rev. Lett.* **92**, 033601 (2004).
[31] Devaux, F., Huy, K. P., Denis, S., Lantz, E., and Moreau, P.-A., "Temporal ghost imaging with pseudothermal speckle light," *J. Opt.* **19**, 024001 (2017).
[32] D'Angelo, M. and Shih, Y., "Quantum imaging," *Laser Phys. Lett.* **2**, 567 (2005).
[33] Shapiro, J. H. and Boyd, R. W., "The physics of ghost imaging," *Quantum Inf. Process.* **11**, 949 (2012).
[34] Schwartz, O., Levitt, J. M., Tenne, R., Itzhakov, S., Deutsch, Z., and Oron, D., "Superresolution microscopy with quantum emitters," *Nano Lett.* **13**, 5832 (2013).
[35] Israel, Y., Tenne, R., Oron, D., and Silberberg, Y., "Quantum correlation enhanced super-resolution localization microscopy enabled by a fibre bundle camera," *Nat. Commun.* **8**, 14786 (2017).
[36] Dertinger, T., Colyer, R., Iyer, G., Weiss, S., and Enderlein, J., "Fast, background-free, 3d super-resolution optical fluctuation imaging (sofi)," *PNAS* **106**, 22287 (2009).
[37] Lemos, G. B., Borish, V., Cole, G. D., Ramelow, S., Lapkiewicz, R., and Zeilinger, A., "Quantum imaging with undetected photons," *Nature* **512**, 409 (2014).
[38] D'Angelo, M., Kim, Y. H., Kulik, S. P., and Shih, Y., "Identifying entanglement using quantum ghost interference and imaging," *Phys. Rev. Lett.* **92**, 233601 (2004).

[39] Scarcelli, G., Zhou, Y., and Shih, Y., "Random delayed-choice quantum eraser via two-photon imaging," *Eur. Phys. J. D* **64**, 167 (2007).
[40] Cassano, M., D'Angelo, M., Garuccio, A., Peng, T., Shih, Y., and Tamma, V., "Spatial interference between pairs of disjoint optical paths with a chaotic source," *Opt. Express* **25**, 6589 (2016).
[41] Genovese, M., "Real applications of quantum imaging," *J. Opt.* **18**, 073002 (2016).
[42] Gatti, A., Bache, M., Magatti, D., Brambilla, E., Ferri, F., and Lugiato, L. A., "Coherent imaging with pseudo-thermal incoherent light," *J. Mod. Opt.* **53**, 739 (2006).
[43] Erkmen, B. I. and Shapiro, J. H., "Signal-to-noise ratio of gaussian-state ghost imaging," *Phys. Rev. A* **79**, 023833 (2009).
[44] O'Sullivan, M. N., Chan, K. W. C., and Boyd, R. W., "Comparison of the signal-to-noise characteristics of quantum versus thermal ghost imaging," *Phys. Rev. A* **82**, 053803 (2010).
[45] Brida, G., Chekhova, M. V., Fornaro, G. A., Genovese, M., Lopaeva, E. D., and Berchera, I. R., "Systematic analysis of signal-to-noise ratio in bipartite ghost imaging with classical and quantum light," *Phys. Rev. A* **83**, 063807 (2011).
[46] Katz, O., Bromberg, Y., and Silberberg, Y., "Compressive ghost imaging," *Appl. Phys. Lett.* **95**, 131110 (2009).
[47] Welsh, S. S., Edgar, M. P., Jonathan, P., Sun, B., and Padgett, M. J., "Multi-wavelength compressive computational ghost imaging," *Proc. SPIE* **8618**, 86180I–1 (2013).
[48] Ferri, F., Magatti, D., Lugiato, L. A., and Gatti, A., "Differential ghost imaging," *Phys. Rev. Lett.* **104**, 104 (2010).
[49] Scala, G., D'Angelo, M., Garuccio, A., Pascazio, S., and Pepe, F. V., "Signal-to-noise properties of correlation plenoptic imaging with chaotic light," *Phys. Rev. A* **99**, 053808 (2019).
[50] Mandel, L. and Wolf, E., [*Optical Coherence and Quantum Optics*], Cambridge University Press, Cambridge (1995).
[51] Isserlis, L., "On a formula for the product-moment coefficient of any order of a normal frequency distribution in any number of variables," *Biometrika* **12**, 134 (1918).
[52] Goodman, J. W., [*Introduction to Fourier Optics*], McGraw-Hill, New York (1996).